Nanoscale Advances

ROYAL SOCIETY OF CHEMISTRY

PAPER

View Article Online
View Journal | View Issue

Cite this: *Nanoscale Adv.*, 2025, **7**, 4067

Self-powered, ultrabroad band photodetectors with large open circuit voltage using colloidal PbSe QDs†

Yuquan Chen,‡[ab] Chandrasekar Perumalveeramalai,‡[b] Chuanbo Li,[a] S. V. N. Pammi,[c] Jagadeesh Babu Bellam,[b] Xiaoming Zhang*[a] and Peipei Ma*[d]

Broad band photodetectors are found to be the inevitable component both in scientific and industrial fields. Here, PbSe colloidal QDs prepared by a simple, inexpensive hot injection method were used to fabricate ultra-broadband photodetectors with visible to near-infrared sensing capabilities. The as-fabricated photodetector has a wide spectral response and a stable photoelectric response to lasers with wavelengths ranging from 405 nm to 1550 nm. The responsivity of the photovoltaic detector is 1.43 mA W^{-1} at 405 nm, 4.67 mA W^{-1} at 980 nm and 0.2 mA W^{-1} at 1550 nm. The device with the optimized structure provides the maximum V_{oc} of 250 mV under 780 nm light illumination and 100 mV even under 1550 nm illumination. Specifically, the detectivity value reaches up to 4.54 × 10^9 Jones under 1550 nm laser illumination with an intensity of 0.41 mW cm^{-2}. As a result, the current study's findings serve as the foundation for the creation of a broad band photodetector that can detect light in the visible to near infrared range.

Received 20th January 2025
Accepted 28th April 2025

DOI: 10.1039/d5na00073d

rsc.li/nanoscale-advances

1. Introduction

In the realm of photoelectric detection, the branch of broad band photodetection holds significant importance in the fields of memory storage, broad band communication and optoelectronic systems.[1] Although broad band photodetectors show a wide range of application prospects in many fields, their research and development still faces a series of challenges, including improving detection efficiency, reducing energy consumption, and optimizing the cost–benefit ratio.[2,3] Until now, separate PDs have been used to cover the sensing of individual sub-bands from the UV to IR range. For example, InGaAs-based PDs are used to sense the NIR region and PbS-based PDs are used for covering mid-IR light.[4,5] Nevertheless, aside from their fabrication challenges, the superior performance of the PDs mentioned above was only obtained at low temperatures. Therefore, necessity of room temperature operatable broad band PDs is always in demand. Moreover, an individual layer comprising lead chalcogenide-based PDs exhibits mostly a narrow wavelength range response.[6,7] Therefore, it is of great significance to study the working principle, material properties and device design of broad band photodetectors for promoting their technological progress and expanding their application range. Furthermore, photodetectors operating under an external bias voltage are directly linked to significant gains in performance and efficiency, while the commercialization of devices is indirectly related to size and packaging challenges. Researchers are currently very interested in studying photodetectors that operate without an external power source, so called self-powered devices, for use in wireless communication and remote sensing applications, particularly in agriculture, civil engineering and Internet of Things (IoTs).[8]

Among the chalcogenide-based semiconducting materials, the PbSe's large exciton Bohr radius of ~46 nm makes it possible to tune the band gap from 0.26 eV to 2 eV by adjusting the size of the nanoparticles and the synthesis parameters.[9,10] Through the utilization of superior absorption properties of PbSe QDs dictated by size, their heterojunction with inorganic materials may improve PD performance metrics and give them a self-powered nature. For instance, S. Peng *et al.* reported the realization of the p–n heterojunction with the La-doped PbSe thin film and 2D-WSe_2 and achieved a stable and continuous response from 405 nm to 1550 nm under 0 V bias.[11] R. Schwanninger *et al.* demonstrated a mid-infrared photodetector (2710–4250 nm) with a high responsivity of 375 A/W using the sintered PbSe/PbS heterojunction structure with the metallic meta-surface absorber.[12] Moreover, a photomultiplication effect was introduced by double layer PbSe CQD films and the detection range was extended from the ultra violet (350 nm) to mid-

[a]*Optoelectronics Research Centre, School of Science, Minzu University of China, Beijing 100081, China. E-mail: xmzhang@muc.edu.cn*

[b]*Department of Physics, Madanapalle Institute of Technology & Science, Madanapalle, Andhra Pradesh, 517 325, India*

[c]*Department of Physics, Sreenidhi University, Ghatkesar, Hyderabad, Telangana 501301, India*

[d]*School of Integrated Circuits, North China University of Technology, Beijing 100144, China. E-mail: mapeipei@ncut.edu.cn*

† Electronic supplementary information (ESI) available. See DOI: https://doi.org/10.1039/d5na00073d

‡ Contributed equally.

infrared region (2500 nm).[13] However, it's always intriguing to see self-powered PDs with a wide spectral range especially those that extend into the NIR region. In order to demonstrate such broad band self-powered PDs, chalcogenides were integrated with other materials to improve the absorption characteristics (related to key performance) and manipulate the band alignment to induce the intrinsic electric field (related to self-powered operation).[11] In a different strategy, broad band self-powered PDs would be realized through the careful selection of the electron transport layer (ETL), hole transport layer (HTL), and electrodes with suitable work function to create an intrinsic built-in electric field for charge carrier separation and transportation. A large band offset between neighboring layers would significantly lower the dark current, and the built-in electric field between the layers would make it easier for charge carriers to move to the electrodes.[14,15] For interface engineering research, the next step would be to analyze charge carrier recombination and band offset behavior at the interface. Recently, solution processed CuSCN was used as the hole transport layer to fabricate a PbS-based photodiode aimed to reduce the dark current and enhance the photoresponsivity by providing the energy barrier between PbS and the anode.[16]

In this work, we have demonstrated a photovoltaic mode (self-powered)-operated photodetector (PVPD) using colloidal PbSe QDs as the photoactive layer in a vertically stacked structure with ZnO as the electron transport layer (ETL) and CuSCN as the hole transport layer (HTL). Broad photoresponse behavior from 405 nm to 1550 nm and response in milliseconds were demonstrated by the vertically stacked PVPD with device structure ITO/ZnO/PbSe QDs/CuSCN/Ag. The vertically stacked PD shows excellent photoresponsivity and specific detectivity under 0 V bias (*i.e.* self-powered) by exploiting the unique interfacial properties of ZnO/PbSe and PbSe/CuSCN heterojunctions. Overall, the PVPD device shows a photoresponsivity of 1.43 mA W^{-1} at 405 nm and 0.2 mA W^{-1} at 1550 nm under 0 V bias conditions. The enhanced and broad spectral responses of the PDs were discussed briefly.

2. Experimental section

2.1. Materials

Selenium powder (Se, 99.9%), tri-*n*-octylphosphine (Top, 90%), oleic acid (OA, AR), 1-octadecene (ODE,>90.0%), *n*-hexane (≥99%), isopropyl alcohol (≥99.9%), *n*-octane (>99%) and diethyl sulfide (≥98%) were purchased from Macklin Chemical Reagent Factory in China. Yellow lead oxide (PbO, 99.999%), tetrabutylammonium iodide (99%), methanol (99.5%), zinc acetate dihydrate (≥98%), potassium hydroxide (99.999%), trichloromethane (>99%) and cuprous thiocyanate (99%) were purchased from Aladdin Chemical Reagent Factory in China. Acetone (99.5%) was purchased from Tianjin Jindong Tianzheng Fine Chemical Reagent Factory in China.

2.2. Synthesis of PbSe quantum dots

First, a Se-TOP precursor solution was prepared by dissolving 2.56 g of selenium powder (Se) in 25.6 mL of tri-*n*-octylphosphine (TOP). The mixture was then stirred for ten minutes, and then it was subjected to ten minutes of ultrasonic treatment. This process was repeated three times until the selenium powder was completely dissolved into a transparent, colorless solution. Subsequently, the lead oleate precursor was synthesized by adding 3.57 g of lead oxide (PbO) powder in a three-neck flask, and 65.12 mL of 1-octaecene (ODE) and 10.8 mL of oleic acid (OA) were added to the three-neck flask, and the flask was then heated to 180 °C in an anhydrous and anaerobic environment. Se-TOP solution was swiftly injected and the temperature was quickly raised to roughly 160 °C after 15 minutes. Following a growth period, the heating apparatus was turned off, and 20 mL of *n*-hexane were injected to quench the solution before it was naturally allowed to cool to room temperature. To boost the stability of the QDs, 8 mL of a 15 mg mL^{-1} ammonium chloride-methanol solution is injected into the solution when the temperature drops to 60 °C. Ultimately, the QDs undergo separation, purification, and cleaning using an acetone and isopropyl alcohol mixture.

2.3. Device fabrication

2.3.1. Self-powered photovoltaic detectors. The vertically stacked PD with device structure ITO/ZnO/PbSe/CuSCN/Ag was fabricated by solution processing. First, ZnO QDs were spin coated on patterned ITO glass substrates with a speed of 3000 rpm for 30 s (three layers) and dried at 70 °C for 30 minutes. Subsequently, PbSe QD layers (size of the QD is ~5.62 nm) were deposited by spin coating with a speed of 2500 rpm, 30 s. The spin coating procedure was repeated (five times) to obtain the desired thickness. Following the completion of each layer, the ligand exchange procedure was conducted using a TBAI-methanol solution, and the sample was then dried for 60 minutes at 40 °C. The CuSCN precursor was prepared by dissolving 70 mg of cuprous thiocyanate (CuSCN) powder in 2 mL of diethyl sulfide. After 20 minutes of ultrasonic treatment, the CuSCN was fully dissolved, yielding a 35 mg mL^{-1} transparent, pale yellow solution. The CuSCN layer was deposited by spin coating for 30 seconds at 2000 rpm. Lastly, the top Ag electrode, which has a thickness of 80 nm, was deposited by vacuum evaporation, and the device size was determined by using a shadow mask.

2.4. Characterization

The structural, morphological, and optical properties of the as-synthesized QDs were analyzed through characterization. The powder X-ray diffraction (XRD) pattern was acquired with a XD-3 diffractometer using monochromatic Cu Kα radiation (λ = 1.54056 Å), 36 kV and 20 mA. The surface morphology of the as-synthesized QDs was obtained by scanning electron microscopy (SEM) with an S-4800 (FESEM). Transmission electron microscopy (TEM) studies were performed using a Tecnai G2 F20 high resolution transmission electron microscope. X-ray photoelectron spectroscopy (XPS) was performed using a Thermo escalab 250Xi. The optical absorption characteristics of QDs were analyzed by using a UV-3600 plus UV-vis-NIR spectrophotometer. The photoelectric properties of the device were measured

by using a keithly 4200 SCS system. Laser diode light sources with different wavelengths (405 nm, 650 nm, 780 nm, 850 nm, 980 nm and 1550 nm) were used for the illumination of the device to measure the photocurrent with adjustable power. A Thorlab power meter was used to measure the illumination intensity.

3. Results and discussion

Fig. 1a shows the XRD pattern of the as-synthesized PbSe QD thin films with a growth time of 200 s and Fig. S1 (ESI†) shows QDs with varying growth times. The PbSe QDs have obvious diffraction peaks at 2θ values of 25.13°, 29.11°, 41.68°, 49.24°, 51.65°, 60.41°, 66.40°, and 68.41° corresponding to the (111), (200), (220), (311), (222), (400), (331), (420) and (422) crystal planes of bulk PbSe, respectively (PDF# 77-0245), of the face centered cubic rock salt structured PbSe crystal. It is noteworthy that the broadening of diffraction peaks indicates that an increase in growth time was associated with an increase in QD size. Overall, the XRD pattern shows that the sample's peak position agrees well with the standard card and that there is no noticeable miscellaneous peak, suggesting a high level of purity.

Furthermore, the structural properties of the as-synthesized PbSe QDs were analyzed by characterizing with HRTEM. The HRTEM image of PbSe QDs synthesized for a growth time of 200 s is shown in Fig. 1b, and the corresponding size distribution plot is shown in the inset, indicating that monodispersed QDs were observed with high crystallinity and a spherical shape. It can be observed that with the increase of reaction time, the size of the quantum dots increases, but the shape is basically similar without a significant change as shown from the HRTEM image in Fig. S2 (ESI).† Additionally, the size increase of QDs, as shown by HRTEM and size distribution analysis from Fig. S2 and S3,† supported the broadening of the XRD peaks. The measured average particle size of QDs with growth times of 60, 120, 200, and 300 seconds is 4.82 nm, 5.14 nm, 5.62 nm, and 6.21 nm, respectively, based on HRTEM and size distribution analysis.

The ability of CQDs to absorb light can be directly reflected by their absorption spectrum, which makes it a valuable tool for researching their photoelectric characteristics. According to Fig. 1c and S4,† 1417 nm, 1465 nm, 1588 nm, and 1704 nm are the first exciton absorption peaks, which correspond to PbSe QDs with growth times of 60 s, 120 s, 200 s, and 300 s, respectively. The absorption peak is redshifted and the QD size increases with increasing reaction time. This is because the absorption peak shifts to a longer wavelength as a result of the weakening of the particle's quantum limiting effect and the reduction of the energy level difference caused by an increase in particle size.[17] Therefore, the band gap of PbSe QDs was tuned from 0.87 eV to 0.72 eV.

The stoichiometric composition and elemental states of as synthesized PbSe QDs were analyzed by X-ray photoelectron spectroscopy. Fig. 1d presents the survey spectrum of PbSe QDs synthesized for 200 s (~5.62 nm), where peaks related to Pb, Se, oxygen and carbon elements were observed. The high-

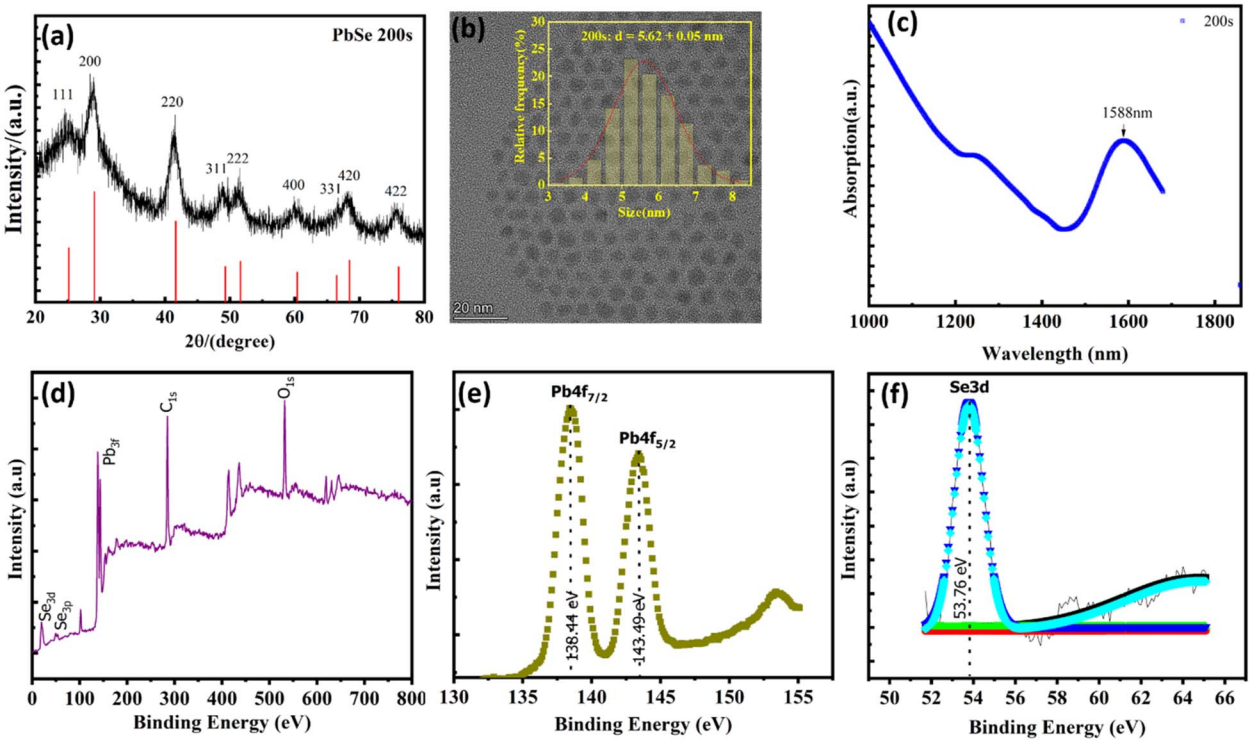

Fig. 1 (a) X-ray diffraction pattern of PbSe QDs; (b) HRTEM image of PbSe QDs synthesized with a growth time of 200 s (inset shows the size distribution plot); (c) UV-vis-IR spectra of PbSe QDs; (d) XPS survey spectrum of PbSe QDs; (e) high resolution XPS spectrum of Pb4f; (f) high resolution XPS spectrum of Se3d.

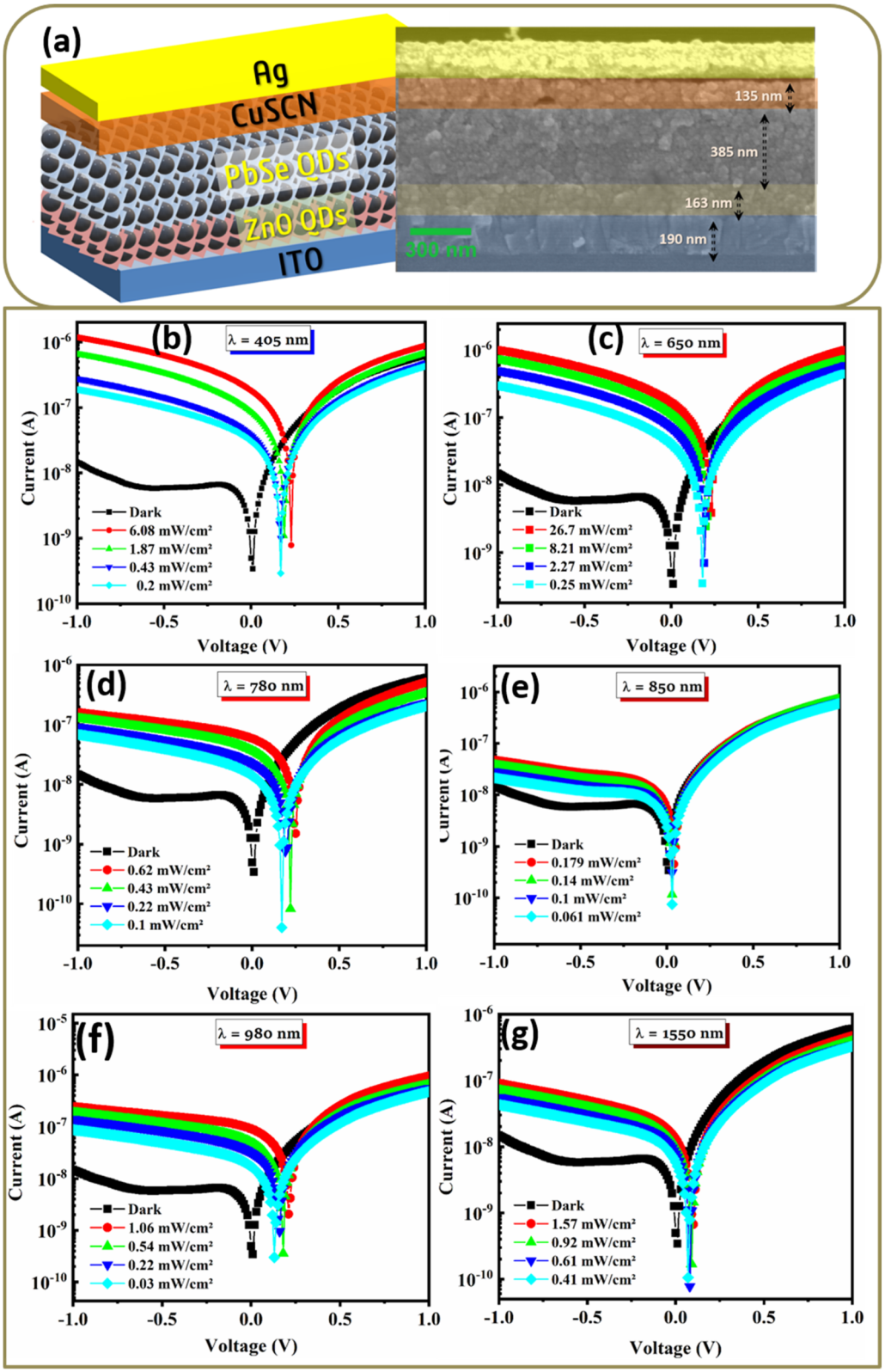

Fig. 2 (a) Schematic illustration of the photovoltaic PD (left side) and cross-sectional FESEM image of the PD with device structure ITO/ZnO (163 nm)/PbSe QDs (385 nm)/CuSCN (135 nm)/Ag (right side); *I*–*V* plot of the PD at various optical power densities under (b) 405 nm, (c) 650 nm, (d) 780 nm, (e) 850 nm, (f) 980 nm and (g) 1550 nm illumination.

resolution XPS spectra of Pb and Se elements are shown in Fig. 1e and f, respectively. The Pb4f peak's doublet feature was clearly visible at a binding energy of 138.4 eV, which corresponds to the $Pb4f_{7/2}$ core level, and 143.0 eV, which corresponds to the $Pb4f_{5/2}$ core level of Pb^{2+} cations. The 5 eV BE difference indicates that the Pb atoms have strong binding.[18] Fig. 1f shows that the strong core level of the peak of Se atom corresponds to the Se5d core level of Se^{2-} ions. From the XPS spectra, the stoichiometric composition of PbSe QDs was determined. The Pb : Se atomic ratio of 1 : 0.8 indicates the deficiency of Se content in PbSe QDs.

In order to exploit the advantage of as-synthesized PbSe QDs, we have fabricated the photovoltaic PD (PVPD) with device structure ITO/ZnO/PbSe QDs/CuSCN/Ag. Fig. 2a shows the schematic figure of the device structure and high resolution FESEM image cross-section of the device with a clear interface structure. The thickness of the ZnO electron transport layer (ETL), photoactive layer, and CuSCN hole transport layer (HTL) was optimized to 163 nm, 385 nm, and 135 nm, respectively. The optoelectronic performance of PVPD was investigated systematically by illuminating with different wavelength light sources from visible to near infrared (NIR) and under various illumination intensities. The scanning voltage is set to −1 V to +1 V, and the *I–V* characteristic curve of the device under dark conditions and under illumination with a 405 nm laser source is shown in Fig. 2b. Under dark conditions, apparently the device has shown strong rectifying behavior with a rectification ratio of 35 at ±1 V. With an open circuit voltage of 250 mV and a short circuit current of 1.8×10^{-7} A, the device exhibits a clear photovoltaic effect when illuminated using a 405 nm laser source with an optical power density 6.08 mW cm^{-2}. The estimated on/off ratio of $\sim 10^3$ indicates the high sensitivity of the PVPD for visible light detection. The offset voltage enables the PD to be operated without a power source (*i.e.* self-powered). In addition, the broad band response of the PVPD was demonstrated by illuminating the detector with lasers of different wavelengths and different optical power densities. The measured *I–V* characteristic curve is shown in Fig. 2c–g. The *I–V* plots under lighting conditions clearly show the photovoltaic features, with the photocurrent increasing gradually as the intensity of the illumination increases, and with an obvious shifting of the curve from 0 V.

It is well known that the open circuit voltage (V_{oc}), in conjunction with the short circuit current and fill factor, is one of the parameters used to assess the efficiency of solar cells.[19] V_{oc} is reportedly mostly dependent on the electronic states at the heterojunction interface.[20] In other words, the magnitude of V_{oc} will thus be determined by the Fermi energy level, valence band maximum, and charge recombination mechanism at the interface.[21] It is noteworthy that even the best depleted heterojunction solar cells have shown an open circuit voltage of less than 500 mV, where the metal oxide interface plays a unique role to decide the V_{oc}.[22] Therefore, the determination of V_{oc} explains the existence of the built-in potential at the interface of the heterojunction device, which in turn explains the self-powered mode operation of PDs. For any device structure, the V_{oc} is mainly controlled by the defect state density of the device. As illustrated in Fig. 3a, both the power density and the wavelength of the light radiation have a significant impact on the V_{oc}. It is observed that the V_{oc} increases invariably with wavelength and logarithmically with light power density. The dependence of V_{oc} on light power density is expressed using the following equation:

$$V_{oc}/q = E_g + n_{ID}\, kT \log(I/I_0)$$

where E_g is the bandgap, q is the elementary charge, k is the Boltzmann constant, T is the absolute temperature, and n_{ID} is the ideality factor. The ideality factor is directly related to the recombination mechanism that occurred at the interface.[23] The ideality factor at different wavelengths is tabulated in Table S1.† The n_{ID} shows the value of 1.81 and 1.89 for 980 nm and 1550 nm, which suggested that the Shockley–Read–Hall (SRH) recombination mechanism dominates due to intragap defects at V_{oc}.[24,25]

It is important to carefully extract the energy levels of each functional layer, in this case ZnO, PbSe, and CuSCN, in order to provide a clear picture of the charge transport mechanism. The band gaps of ZnO, PbSe and CuSCN layers were estimated from the absorption spectra and their corresponding Tauc plot as shown in Fig. S5 (ESI).† The Tauc plot was obtained by plotting $(\alpha h\nu)^2$ V s $h\nu$ and the band gaps of ZnO, PbSe and CuSCN were calculated to be 3.49 eV, 0.75 eV and 3.89 eV, respectively. As illustrated in Fig. S6(a–i)†, the parameters such as work function, valence band maximum (VB), and conduction band minimum (CB) of the layers to establish the energy levels of ZnO, PbSe and CuSCN were extracted from the corresponding UPS spectrum. For ZnO, PbSe, and CuSCN, respectively, the effective work function of the layers was found to be 4.72, 4.98, and 4.97 eV, which closely agreed with the reported literature.[26] The schematic energy level diagrams of PVPD layers before contact and after contact under light illumination are depicted in Fig. 3b–d. From the figure, the charge transport mechanism of our device has been picturized as follows: prior to contact, ZnO, PbSe, and CuSCN have distinct Fermi energies under dark conditions. The UPS measurement yielded the E_F values of ZnO, PbSe, and CuSCN, which are 4.72 eV, 4.97 eV, and 4.98 eV, respectively. When they come into contact, the EF levels tend to align in the same level by the transfer of electrons from PbSe to ZnO and transfer of holes from ZnO to PbSe, which constitute the internal built-in electric field. The built-in electric field is having the direction from ZnO to PbSe. Similarly, the E_F levels of CuSCN (4.98 eV) and PbSe ($E_F \sim 4.97$ eV) align each other, which creates the built-in electric field. Under light illumination, excitons (electron–hole pairs) are generated, which are separated by the built-in electric field and move to the respective electrodes.[27,28] Therefore, our device with an optimized structure provides the maximum V_{oc} of 250 mV under 780 nm light illumination. It is noteworthy that our device was able to produce a voltage of 100 mV even under 1550 nm illumination, demonstrating its superiority. Overall, operational capability at 0 V bias from 405 nm to 1550 nm (visible to infrared region) makes our device feasible for broad band application.

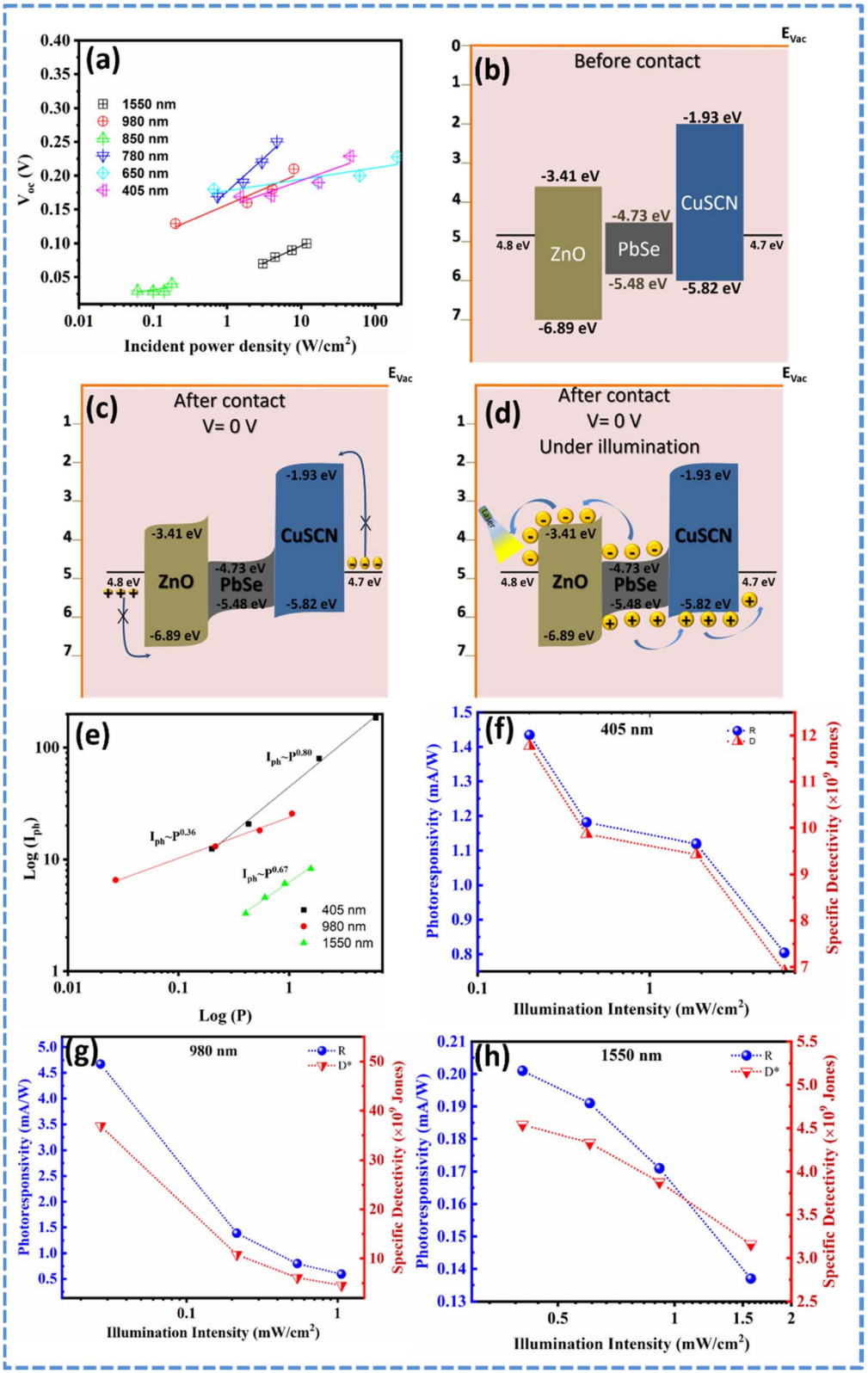

Fig. 3 (a) Dependence of open circuit voltage (V_{oc}) on incident power density at different wavelengths of irradiation. The energy level band diagram of the PVPD with structure ITO/ZnO/PbSe/CuSCN/Ag, (b) before contact, (c) after contact, (d) after contact under illumination at 0 V bias; (e) dependence of photocurrent on incident power density under 405 nm, 980 nm and 1550 nm light illumination; dependence of photoresponsivity (R) and specific detectivity (D^*) on illumination intensity under (f) 405 nm, (g) 980 nm, and (h) 1550 nm light illumination.

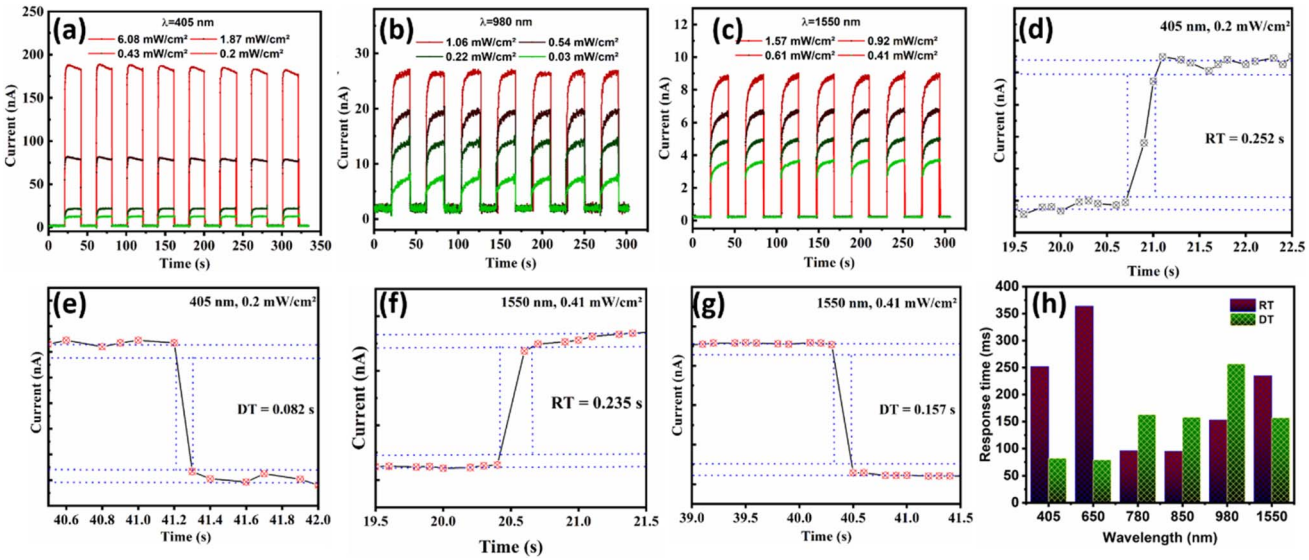

Fig. 4 The dynamic photoresponse characteristic curve of the PVPD at different wavelengths and light power densities (a) 405 nm, (b) 980 nm, and (c) 1550 nm; enlarged portion of the *I*–*t* curve edge on rise (*RT*) and decay time (DT) of PVPD under (d and e) 405 nm and (f and g) 1550 nm illumination; (h) graphical chart for the response time at different wavelengths.

Fig. 3e displays a logarithmic plot of the PVPD photocurrent as a function of incident power. The power law function $I_{ph} \alpha P^m$ was used to fit the curves. Remarkably, for the wavelength of 405 nm, 980 nm and 1550 nm, the exponent m yields the values 0.80, 0.36 and 0.67. The m value actually gets close to the optimal value of 1 for a wavelength of 405 nm, whereas other wavelength yields a lower m value. Because recombination takes place deep within the band gap and the quasi-Fermi level does not cross the recombination centers, this phenomenon is seen in perovskite-inspired materials operating in photovoltaic mode.[29]

Quantitative parameters to take into account when characterizing the PDs include photoresponsivity (R), specific detectivity (D^*), response time (τ_R and τ_D), external quantum efficiency (EQE), and photoconductive gain. The relationship between the incident light power density and the detector's specific detectivity and responsivity is reflected in Fig. 3f–h, respectively. Under 405 nm illumination, our results indicate the formation of an excellent interface between the ETL, HTL and photoactive layer, which is reflected in the sensitivity and photoresponsivity. The typical absorption characteristics of PbSe, which exhibit high absorption in the lower wavelength region, are further demonstrated by a high R of 1.43 mA W^{-1} under 405 nm illumination, which is greater than 0.2 mA W^{-1} under 1550 nm illumination and less than 4.67 mA W^{-1} under 980 nm illumination. The specific detectivity values calculated for the PVPD under 405, 980 and 1550 nm illumination are 1.18×10^{10} Jones, 3.69×10^{10} Jones, and 4.54×10^{10} Jones, respectively. Both the R and D^* values show a trend of decreasing with increasing illumination intensity. This phenomenon in our PDs indicates that at low illumination intensity, the photogenerated carriers are mostly captured by

Table 1 The key parameter comparison table for chalcogenide-based photodetectors

Device structure	Detection wavelength (nm)	Bias condition (V)	Photoresponsivity (mA W^{-1})	Detectivity (Jones)	Response time	Ref.
Au/PbS superlattice/Au	1550	1	1.44×10^3	5.8×10^{10}	100 ms/123 ms	31
FTO/TiO_2/PbS/CuSCN/Ag		1		5×10^{10}	50 μs/110 μs	16
Cr/PbSe/Cr	1550	0		1.13×10^9		32
Au/PbSe/Au	1000–4000	10	10	—	140 ms/120 ms	33
Cr/Au/PbSe/Cr/Au	2700	0	6.6×10^{-3}	6.6×10^7		34
Au/CdS/PbSe/Au	4700	0	55	5.48×10^8		35
FTO/ZnO/EDT-PbSe/TBAI-PbSe/MoO_3/Ag	1500–2500	−1	100	$\sim 10^{11}$	140/410 μs	13
Pt/PbSe QDs/Pt	1520		960	8.13×10^9		36
CdSe/PbSe/ZnS/Au	3500	0	40 000	7.5×10^9	—	
Au/PbSe CQDs/CdS/CdSe: In/Si	4200		360	8.5×10^8	—	37
ITO/ZnO/PbSe/CuSCN/Ag	405	0	1.43	1.18×10^{10}	252 ms/82 ms	This work
	1550	0	0.20	4.54×10^9	235 ms/157 ms	

the trap states and consequently the electron–hole recombination is reduced.[30] On the other hand, a relatively small proportion of the photogenerated carriers are captured by the trap states at high illumination intensity. Therefore, the device reacted more sensitively to the low intensity of incident light. The number of photons on the detector per unit of time decreases with decreasing optical power density, and each photon has the capacity to excite an electron–hole pair. Because of this, there are fewer electron–hole pairs formed by photons, and as a result, there are fewer excited electron–hole pairs, which lowers the photogenerated current flowing through the detector and lowers the switching ratio.

The optical response characteristics of the detector were investigated by testing the PVPD's *I–t* curve under different optical power densities with different wavelength light sources at 0 V bias. As portrayed in Fig. 4a–c, regardless of the illumination wavelength (405 nm, 980 nm, and 1550 nm), the maximum photocurrent was found to be unaltered, indicating the highly reproducible over long operation period and stable characteristics of the device. Furthermore, the PD's response and recovery times are essential parameters for validation before practical application. The magnified edge of the ON and OFF cycle of the *I–t* curve measured under 405 nm illumination is shown in Fig. 4d and e. The PVPD shows 252 and 82 ms for the rising and decaying times, respectively. These times are defined as the amount of time needed for the photocurrent to increase from minimum to 90% of the maximum photocurrent and to decrease from maximum to 10% of the maximum photocurrent. The response time of the PVPD under 1550 nm illumination is also measured as shown in Fig. 4f and g, which yields 235 ms and 157 ms. Actually, our device's measured response time ought to be lower because it has been constrained by metrics like the laser source switching speed. The summary of the response time in the broad spectral range is graphically displayed in Fig. 4h. The response time is significantly shorter than with the PCPD, which is associated with the short charge carrier path that the PD design offers.[34] The comparison of key parameters with PbSe-based photodetectors is given in Table 1. It is evident that our device responds rapidly to light in the visible to infrared range, making it appropriate for wide-band optoelectronic applications.

4. Conclusion

In brief, PbSe colloidal QDs with superior monodispersity, consistent size, and superior structural quality were synthesized using a hot injection technique. The as-synthesized QDs exhibit a redshift phenomenon, the absorption peak of the first exciton varies from 1417 nm to 1704 nm, and the absorption spectra demonstrate that the particle size increases gradually with the increase in reaction time. As the light absorption layer, PbSe QDs with an absorption peak of 1588 nm were selected in order to fabricate the photodetector. The photovoltaic mode detector with device structure ZnO/PbSe/CuSCN exhibits photoresponsivity of 1.43 mA W^{-1} at 405 nm, 4.67 mA W^{-1} at 980 nm and 0.2 mA W^{-1} at 1550 nm, respectively. Furthermore, the photovoltaic detectors' specific detectivity and response time, which are important figures of merit parameters, were on par with or superior to the PDs that were published, particularly in broad band spectral mode. Hence, the research results have led to significant progress in the application of PbSe QDs in high-performance photodetectors with a broad spectral range.

Data availability

The data supporting this article have been included as part of the ESI.†

Conflicts of interest

There are no conflicts to declare.

Acknowledgements

This work was supported by the National Natural Science Foundation of China (Grant No. 62274190, 12174462, and 62101612) and the international collaboration project of Ministry of Science and Technology (Grant No. QN2023184003L).

References

1 E. Wu, D. Wu, C. Jia, Y. Wang, H. Yuan, L. Zeng, T. Xu, Z. Shi, Y. Tian and X. Li, In Situ Fabrication of 2D WS2/Si Type-II Heterojunction for Self-Powered Broadband Photodetector with Response up to Mid-Infrared, *ACS Photonics*, 2019, **6**, 565–572.
2 W. Zhou, R. Xu, H. Wu, X. Jiang, H. Wang, F. P. García de Arquer and Z. Ning, Quantum-Tuned Cascade Multijunction Infrared Photodetector, *ACS Nano*, 2023, **17**, 18864–18872.
3 H. Li and Z. Yang, Recent progress in mid-infrared photodetection devices using 2D/nD (n = 0, 1, 2, 3) heterostructures, *Mater. Des.*, 2023, **225**, 111446.
4 A. Rogalski, HgCdTe infrared detector material: history, status and outlook, *Rep. Prog. Phys.*, 2005, **68**, 2267.
5 A. Rogalski, J. Antoszewski and L. Faraone, Third-generation infrared photodetector arrays, *J. Appl. Phys.*, 2009, **105**, 091101.
6 Z. Lin, Z. Yang, P. Wang, G. Wei, A. He, W. Guo and M. Wang, Schottky–ohmic converted contact, fast-response, infrared PbTe photodetector with stable photoresponse in air, *RSC Adv.*, 2016, **6**, 107878–107885.
7 K. Qiao, H. Deng, X. Yang, D. Dong, M. Li, L. Hu, H. Liu, H. Song and J. Tang, Spectra-selective PbS quantum dot infrared photodetectors, *Nanoscale*, 2016, **8**, 7137–7143.
8 K. S. R. B, S. Panda, E. Ramasamy, S. Badhulika, G. Veerappan and P. H. Borse, Fabrication of a self-powered broadband photodetector by 50% replacement of Pb by Mg in the $CH_3NH_3Pb_{0.5}Mg_{0.5}Cl_2I$ perovskite lattice, *Mater. Adv.*, 2023, **4**, 6522–6534.
9 M. Shandalov and Y. Golan, Microstructure and morphology evolution in chemical solution deposited semiconductor

films: 2. PbSe on As face of GaAs(111), *Eur. Phys. J.:Appl. Phys.*, 2004, **28**, 51–57.

10 T. Aubert, A. A. Golovatenko, M. Samoli, L. Lermusiaux, T. Zinn, B. Abécassis, A. V. Rodina and Z. Hens, General Expression for the Size-Dependent Optical Properties of Quantum Dots, *Nano Lett.*, 2022, **22**, 1778–1785.

11 S. Peng, C. Zhang, X. Liu, J. Han, C. Li, H. Zhou, H. Yu, C. Chen, J. Gou and J. Wang, Self-Powered and Broadband Photodetector with High Responsivity and Fast Response Based on La-Doped PbSe Film Heterojunction, *ACS Photonics*, 2024, **11**, 2604–2614.

12 R. Schwanninger, S. M. Koepfli, O. Yarema, A. Dorodnyy, M. Yarema, A. Moser, S. Nashashibi, Y. Fedoryshyn, V. Wood and J. Leuthold, Highly Responsive Mid-Infrared Metamaterial Enhanced Heterostructure Photodetector Formed out of Sintered PbSe/PbS Colloidal Quantum Dots, *ACS Appl. Mater. Interfaces*, 2023, **15**, 10847–10857.

13 T. Zhu, L. Zheng, X. Yao, L. Liu, F. Huang, Y. Cao and X. Gong, Ultrasensitive Solution-Processed Broadband PbSe Photodetectors through Photomultiplication Effect, *ACS Appl. Mater. Interfaces*, 2019, **11**, 9205–9212.

14 J. Li, D. Wang, X. Chen, Y. Zhou, H. Luo, T. Zhao, S. Hu, Z. Zheng, W. Gao and X. Liu, Engineering energy bands in 0D–2D hybrid photodetectors: Cu-doped InP quantum dots on a type-III SnSe2/$MoTe_2$ heterojunction, *Nanoscale Horiz.*, 2025, **10**, 922–932.

15 J. Na, Y. Kim, J. H. Smet, M. Burghard and K. Kern, Gate-Tunable Tunneling Transistor Based on a Thin Black Phosphorus–$SnSe_2$ Heterostructure, *ACS Appl. Mater. Interfaces*, 2019, **11**, 20973–20978.

16 I. Ka, L. F. Gerlein, I. M. Asuo, S. Bouzidi, D. M. Gedamu, A. Pignolet, F. Rosei, R. Nechache and S. G. Cloutier, Solution-Processed p-Type Copper Thiocyanate (CuSCN) Enhanced Sensitivity of PbS-Quantum-Dots-Based Photodiode, *ACS Photonics*, 2020, **7**, 1628–1635.

17 O. E. Semonin, J. M. Luther and M. C. Beard, Quantum dots for next-generation photovoltaics, *Mater. Today*, 2012, **15**, 508–515.

18 J.-J. Zhu, H. Wang, S. Xu and H.-Y. Chen, Sonochemical Method for the Preparation of Monodisperse Spherical and Rectangular Lead Selenide Nanoparticles, *Langmuir*, 2002, **18**, 3306–3310.

19 K. L. Mutolo, E. I. Mayo, B. P. Rand, S. R. Forrest and M. E. Thompson, Enhanced Open-Circuit Voltage in Subphthalocyanine/C60 Organic Photovoltaic Cells, *J. Am. Chem. Soc.*, 2006, **128**, 8108–8109.

20 C. J. Brabec, A. Cravino, D. Meissner, N. S. Sariciftci, M. T. Rispens, L. Sanchez, J. C. Hummelen and T. Fromherz, The influence of materials work function on the open circuit voltage of plastic solar cells, *Thin Solid Films*, 2002, **403**, 368–372.

21 H. Choi, J. H. Song, J. Jang, X. D. Mai, S. Kim and S. Jeong, High performance of PbSe/PbS core/shell quantum dot heterojunction solar cells: short circuit current enhancement without the loss of open circuit voltage by shell thickness control, *Nanoscale*, 2015, **7**, 17473–17481.

22 R. L. Z. Hoye, B. Ehrler, M. L. Böhm, D. Muñoz-Rojas, R. M. Altamimi, A. Y. Alyamani, Y. Vaynzof, A. Sadhanala, G. Ercolano, N. C. Greenham, R. H. Friend, J. L. MacManus-Driscoll and K. P. Musselman, Improved Open- Circuit Voltage in ZnO–PbSe Quantum Dot Solar Cells by Understanding and Reducing Losses Arising from the ZnO Conduction Band Tail, *Adv. Energy Mater.*, 2014, **4**, 1301544.

23 W. Tress, M. Yavari, K. Domanski, P. Yadav, B. Niesen, J. P. Correa Baena, A. Hagfeldt and M. Graetzel, Interpretation and evolution of open-circuit voltage, recombination, ideality factor and subgap defect states during reversible light-soaking and irreversible degradation of perovskite solar cells, *Energy Environ. Sci.*, 2018, **11**, 151–165.

24 D. Zheng, C. Tong, T. Zhu, Y. Rong and T. Pauporté, Effects of 5-Ammonium Valeric Acid Iodide as Additive on Methyl Ammonium Lead Iodide Perovskite Solar Cells, *Nanomater*, 2020, **10**, 2512.

25 Z. Dan, B. Yang, Q. Song, J. Chen, H. Li, W. Gao, L. Huang, M. Zhang, M. Yang, Z. Zheng, N. Huo, L. Han and J. Li, Type-II Bi_2O_2Se/$MoTe_2$ van der Waals Heterostructure Photodetectors with High Gate-Modulation Photovoltaic Performance, *ACS Appl. Mater. Interfaces*, 2023, **15**, 18101–18113.

26 Y. Liu, F. Li, G. Shi, Z. Liu, X. Lin, Y. Shi, Y. Chen, X. Meng, Y. Lv, W. Deng, X. Pan and W. Ma, PbSe Quantum Dot Solar Cells Based on Directly Synthesized Semiconductive Inks, *ACS Energy Lett.*, 2020, **5**, 3797–3803.

27 G. Seo, S. Kim, H. Choi and M.-c. Kim, Enhanced performance of lead sulfide quantum dot-sensitized solar cells by controlling the thickness of metal halide perovskite shells, *Heliyon*, 2023, **9**(10), e20276.

28 J. Huang, K. Shu, N. Bu, Y. Yan, T. Zheng, M. Yang, Z. Zheng, N. Huo, J. Li and W. Gao, Reconfigurable WSe_2 Schottky heterojunctions for logic rectifiers and ultrafast photodetectors, *Sci. China Mater.*, 2023, **66**, 4711–4722.

29 J. Mei, M. Liu, P. Vivo and V. Pecunia, Two-Dimensional Antimony-Based Perovskite-Inspired Materials for High-Performance Self-Powered Photodetectors, *Adv. Funct. Mater.*, 2021, **31**, 2106295.

30 L. Gu, M. M. Tavakoli, D. Zhang, Q. Zhang, A. Waleed, Y. Xiao, K.-H. Tsui, Y. Lin, L. Liao, J. Wang and Z. Fan, 3D Arrays of 1024-Pixel Image Sensors based on Lead Halide Perovskite Nanowires, *Adv. Mater.*, 2016, **28**, 9713–9721.

31 C. Wang, Z. Chen, Z. Liu, T. Ma, X. Chen, M. Zhang, D. Luo, B.-R. Hyun and X. Liu, Adjusting Microscale to Atomic-Scale Structural Order in PbS Nanocrystal Superlattice for Enhanced Photodetector Performance, *Small*, 2023, **19**, 2300975.

32 Z. Huan, Q. Lv, M. Yu, R. Li, Z. Huang, G. Liu, G. Qiao and J. Liu, Efficient and stable self-powered PbSe photodetectors *via* doping-induced asymmetric Cr electrodes modulation of surface work function, *Sens. Actuators A: Phys.*, 2024, **370**, 115254.

33 S. Kim, S. Choo, Y. Kim, W. S. Hwang and M. Shin, Comparative study of the near-infrared detection of PbSe

fabricated using a sputter deposition method, *Thin Solid Films*, 2024, **795**, 140313.

34 S. Yan, Q. Yang, S. Feng, J. Shen, J. Yang, L. Tang, C. Leng and D. Zhou, Effect of Air Atmosphere Sensitization on Formation of PbSe p–n Junctions for High-Performance Photodetectors, *J. Electron. Mater.*, 2020, **49**, 4929–4935.

35 B. Weng, J. Qiu, L. Zhao, C. Chang and Z. Shi, CdS/PbSe heterojunction for high temperature mid-infrared photovoltaic detector applications, *Appl. Phys. Lett.*, 2014, **104**, 121111.

36 M. Thambidurai, Y. Jang, A. Shapiro, G. Yuan, H. Xiaonan, Y. Xuechao, Q. J. Wang, E. Lifshitz, H. V. Demir and C. Dang, High performance infrared photodetectors up to 2.8 μm wavelength based on lead selenide colloidal quantum dots, *Opt. Mater. Express*, 2017, **7**, 2326–2335.

37 J. Qiu, B. Weng, L. L. McDowell and Z. Shi, Low-cost uncooled MWIR PbSe quantum dots photodiodes, *RSC Adv.*, 2019, **9**, 42516–42523.